Int. J. Electrochem. Sci., 17 **(2022)** Article Number: 221129, doi: 10.20964/2022.11.08

International Journal of
ELECTROCHEMICAL
SCIENCE
www.electrochemsci.org

In Situ Synthesis of Ultrathin Co_3O_4 Nanoflakes Film on Ni Foam with Enhanced Performance for Electrochemical Oxygen Evolution

Tianyi Gao, Qing Zhang, Yunshuang Ge, Xiaoyu Sun, Zhipeng Ma, Wenfeng Guo[*], *Shengxue Yu and Yuqian Fan*[*]

Department of Applied Chemistry, College of Environmental and Chemical Engineering, Yanshan University, Qinhuangdao 066004, China.
[*]E-mail: wfguo@ysu.edu.cn (W.Guo), yqfan@ysu.edu.cn (Y. Fan)

Received: 17 July 2022 / *Accepted:* 1 September 2022 / *Published:* 10 October 2022

Herein we present a brand-new and straightforward method for producing ultrathin Co_3O_4 nanoflakes directly on a Ni foam (NF) substrate, resulting in a Co_3O_4@NF electrode. An intrinsic cross-linked structure with a flake thickness of about 2.5 nm is created by the anchored ultrathin Co_3O_4 nanoflakes, and it has the advantages of strong affinity, good conductivity, and a large active surface area. Utilized as an additive-free electrode, the substance works admirably in the oxygen evolution reaction (OER) with a low overpotential of 290 mV at 10 mA cm^{-2}, a small Tafel slope of 61.2 mV dec^{-1}, and great durable stability for long-term operating. *In situ* EIS further reveals its intrinsic kinetic characteristics for excellent OER catalytic performance. Besides, A well-established electrolyzer can also produce a current density of 290 mA cm^{-2} at 2 V and has improved long-term stability when using Pt@NF as the cathode and Co_3O_4@NF as the anode. From a methodological perspective, the suggested procedure may be extremely valuable in the synthesis of other efficient catalytic ultrathin nanoparticles (Nps).

Keywords: Co_3O_4, ultrathin nanoflakes, film electrode, oxygen evolution, electrochemical energy conversion.

1. INTRODUCTION

The electrochemical oxygen-related researches, e.g. oxygen evolution reaction (OER) and oxygen reduction reaction (ORR), have attracted tremendous interests in recent years. This is largely because of their significant applications for the storage and/or utilization of renewable energy in industries like water splitting, fuel cells, and rechargeable metal-air batteries. [1-4]. In the case of storing intermittent energy (such as solar, wind and tidal, etc) to chemical fuels, the electrolysis of water is considered to be one of the most ideal strategies which could simultaneously produce H_2/O_2 at

cathode/anode respectively in an electrolytic cell [5-7]. 1.23 V of thermodynamic voltage is required for the electrolysis of water to produce H_2 and O_2. OER, on the other hand, has a more intricate multi-step reaction mechanism involving four protons and electrons. It will induce sluggish kinetics and have an impact on the overall water splitting efficiency. Therefore, in order to account for the reaction barriers, a significant overpotential must be connected to the theoretical voltage [8-10]. The introduction of catalytic electrodes, which might lower the overpotential and quicken the electrochemical process, is crucial to resolving this issue. The development of novel OER catalysts has therefore received a lot of attention during the past ten years, and reports of their increased performance are widespread. It is apparent that noble metal (Pt, Ir, Ru, etc)-based materials exhibit high activities for OER catalysis. Unfortunately, the expensive cost and scarce earth-storage greatly restrict their large-scale commercial application [1, 5, 7, 13, 14]. In light of this circumstance, the development of alternative OER catalysts, such as low-cost transition metal (e.g. Co, Ni, Fe, etc)-based and/or carbon-based materials, is an urgent and challenging work that has a promising prospect [15-18].

It has been shown that spinel cobalt oxide (Co_3O_4), which has Co^{2+} at tetrahedral sites and Co^{3+} at octahedral sites, is a competitive OER catalyst with numerous advantages, including strong electrochemical activity, good stability, a low cost, and earth-abundance. [19-21]. To date, many Co_3O_4 nanoparticles (NPs), such as wires, sheets/flakes, cubes, and 3D products, have been researched for OER catalysis [22-24]. Amongst, Co_3O_4 materials with ultrathin structures (< 5 nm in any dimension) are more desirable because they possess substantial high surface area and thus could make the most of cobalt atoms exposed outside to form catalytic centres [25-27]. The most frequently reported powder ultrathin Co_3O_4 NPs do, however, have the disadvantages of facile aggregation, weak affinity/low conductivity with the substrate, and the requirement for an intricate process for electrode manufacturing by adding additional polymer binders and conducting materials. To overcome these disadvantages, a feasible strategy is directly growing ultrathin Co_3O_4 NPs on electrode substrate [28, 29]. Nonetheless, to our current knowledge, little attention has been paid to this field and few directly anchored ultrathin Co_3O_4 NPs were developed for OER application due to the lack of successful synthetic routes.

Herein, we propose a novel and simple strategy to grow ultrathin Co_3O_4 nanoflakes directly on Ni foam (NF) and obtain a Co_3O_4@NF electrode. The morphological and crystallographic properties of the as-prepared product are deeply investigated. Being adopted as catalytic anode for oxygen evolution, the electrode exhibits enhanced electrochemical catalytic activity, relatively stable durability for long-term running, and moreover, impressive performance in practical application.

2. EXPERIMENTAL SECTION

2.1. Materials synthesis

By using Co layer (on Ni foam (NF) with area of 1×1 cm^2) for product synthesis, the route was composed of a simple oxidation step in aqueous electrolyte and followed by a thermal treatment step in a muffle furnace. All reagents used herein were of analytical grade. The adopted original Co@NF electrode was obtained by an electrodeposition method. For the typical step, a metal Co plate (99.9%)

and a Ni foam (1.7 mm in thickness) were used as cathode and anode, respectively. The electrolyte was composed of 73 g L^{-1} cobalt sulphate ($CoSO_4$•$7H_2O$) and 70 ml L^{-1} triethanolamine (TEA) with pH value adjusted at 3-4. The electro-deposition process was performed under a constant current density of 50 mA cm^{-2} for 3 min at a temperature of 40 °C. Then a Co@NF electrode was obtained with metal Co layer evenly deposited on NF substrate.

For synthesis of anchored ultrathin Co_3O_4 nanoflakes, the as-obtained Co@NF electrode was immersed in a 1M sodium carbonate (Na_2CO_3) electrolyte and kept still in a thermostat at 80 °C for 2 h. During this step, the metal Co layer was gradually oxidized and transformed into a precursor film. After being thoroughly washed by deionized water and dried at room temperature, the obtained precursor electrode was heated to 250 °C at a rate of 2 °C min^{-1} and maintained at 250 °C for 2 h in a muffle furnace. Finally, the synthesized ultrathin Co_3O_4 nanoflakes film was obtained. The loading density of Co_3O_4 film was calculated to be ~0.1 mg cm^{-2}.

2.2. Physical characterizations

The scanning electron microscopy (SEM), energy dispersive spectroscopy (EDS), as well as selected-area electron diffraction (SAED) were measured on a Hitachi S-4800 instrument operated at 5 kV. On a Philips Tecnai G2 F30, transmission electron microscopy (TEM) was performed on the product (operated at 300 kV).

On a Rigaku Smart Lab X-ray diffractometer operated at 40 kV with Cu Kα radiation under a scan rate of 5° min^{-1}, the X-ray diffraction (XRD) pattern was acquired. The X-ray photoelectron spectroscopy (XPS) analysis was carried out using a Thermo ESCALAB 250XI. The Raman spectrum was measured on a Renishaw invia system with an excitation wavelength of 514 nm. On a Shimadzu AUW120D electronic analytical balance (d = 0.01 mg), the weight of the fabricated film product was calculated.

2.3. Electrochemical measurements

The electrochemical oxygen evolution research was accomplished on a three-electrode system by using the as-synthesized Co_3O_4@NF electrode as a working electrode, a graphite plate and Ag/AgCl electrode (in saturated KCl) as counter and reference electrodes, respectively. All electrochemical measurements were carried out on a CHI 660E potentiostat in 6 M KOH solution under room temperature (20 °C). The CV, Linear sweep voltammetry (LSV) and chronoamperometry (CA) measurements were all performed using a CHI 660E potentiostat with iR compensated. The *in situ* EIS test was performed on a Parstat 2273 analyzer with amplitude voltage of 5 mV and a frequency ranging from 100 kHz to 10 mHz. The cathode of the single cell was a Pt@NF electrode, and the spacing between the anode and the cathode was kept constant at 0.5-1 cm. An electro-deposition method was utilized to obtain the Pt@NF electrode using H_2PtCl_6 (Pt concerntration: 1.0 g L^{-1}) as electrolyte with a current density of 2 mA cm^{-2} for 1 h. The mass density was controlled at ~1.6 mg cm^{-2}. The corresponding LSV behavior of Pt@NF electrode for hydrogen evolution is given in Fig. S1. The solar

cell-H_2O splitting electrolyzer station was built by connecting a commercial solar cell (5V,1A) to our single cell using a DC-DC converter.

3. RESULTS AND DISCUSSION

As indicated in Fig. 1a, the typical *in situ* fabrication of Co_3O_4@NF electrode involves a straightforward oxidation step in aqueous electrolyte followed by a heat treatment step. Fig. S2 displays typical digital images of as-obtained product, compared with original Co@NF electrode and bare NF.

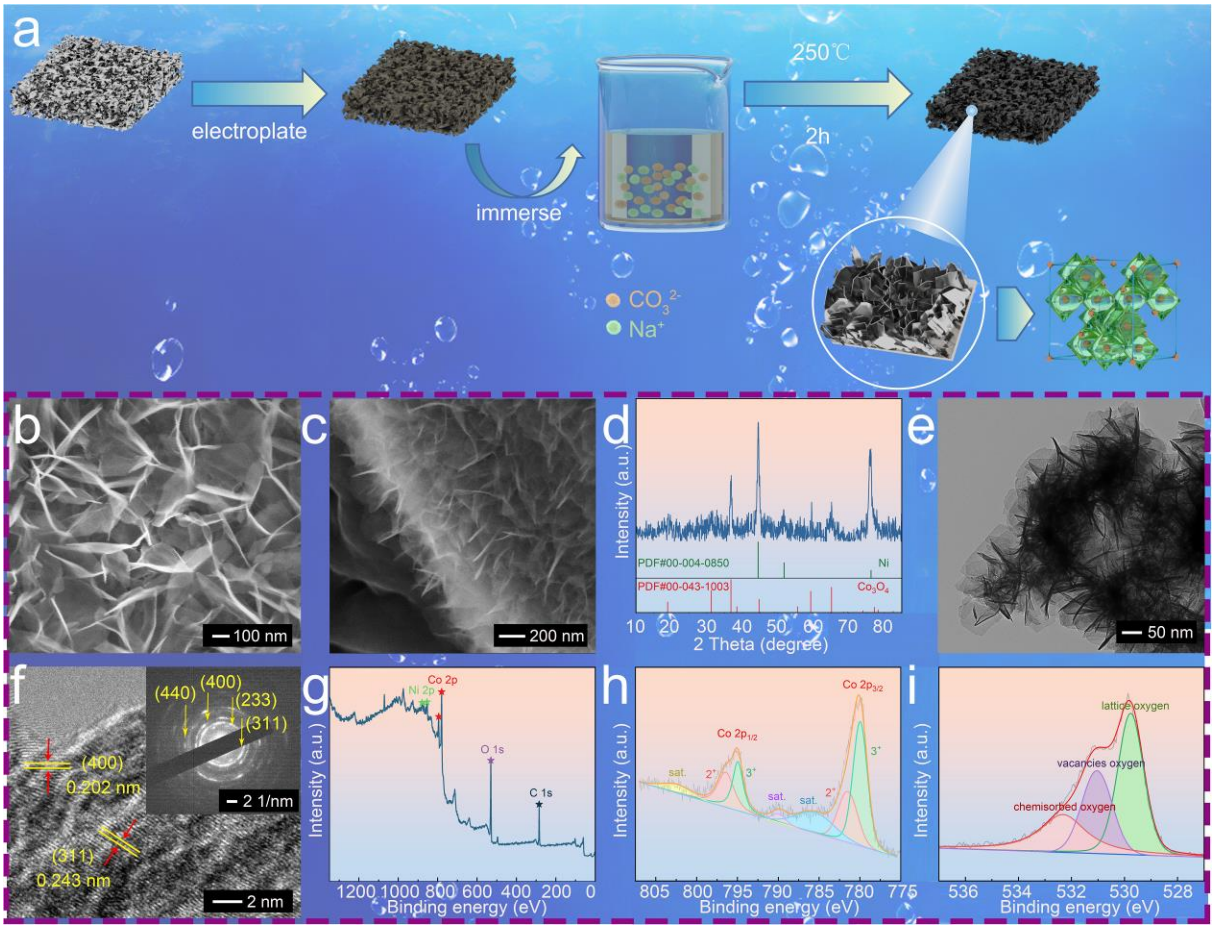

Figure 1. (a) Schematic illustration for the synthesis of the Co_3O_4@NF electrode. (b, c) close front-view and side-view SEM images of as-obtained Co_3O_4 film product. (d) XRD pattern of the Co_3O_4@NF electrode. (e) typical TEM image of Co_3O_4 film product, and (f) HR-TEM image with SAED result (inset in f) of the product. (g) Full XPS spectra and (h, i) high-resolution XPS spectra of Co 2p and O 1s of the product, respectively.

It is obvious that metal Co layer has transformed into a dark film after process. Fig. S3 shows a low-magnification SEM image of the as-synthesized film product for the purpose of analyzing its morphological structure, indicating that the film is composed of a substantial quantity of nanoflakes. For advanced observation, Fig. 1b and Fig. 1c present close front-view and side-view SEM images of film

product, respectively. It is found that the as-grown nanoflakes, without duplicated shape and length, are well anchored on the substrate with a strong affinity. Besides, from Fig. 1b and Fig. 1c, it could be further confirmed that the as-obtained nanoflakes reveal ultrathin thickness implying a large specific surface area, which is desirable for an electrochemical catalytic electrode. The crystallographic structure of the film product was further measured by X-ray diffraction (XRD), and the result is illustrated in Fig. 1d. Three diffraction peaks at two-theta of 44.5, 51.8, and 76.4 (^{o}) are well indexed to metal Ni substrate (PDF # 00-004-0850). Additionally, the other obvious peaks at two-theta of 19.1, 31.3, 36.9, 59.3 as well as 65.2 (^{o}) correspond with the (111), (220), (311), (511), and (440) planes of spinel Co_3O_4 (PDF # 00-043-1003). There is no detected diffraction signal related to metal Co, verifying that the deposited Co layer has completely transformed to Co_3O_4 product. For further validation, the as-synthesized film was evaluated with Raman spectra, as shown in Fig. S4. The observed four strong peaks in Raman spectrum can correspond to the F_{2g} (194 cm^{-1}), E_g (483 cm^{-1}), F_{2g} (523 cm^{-1}), and A_{1g} (693 cm^{-1}) modes of a Co_3O_4 spinel according to previous reports [30]. Thus, by combining the Raman result and XRD investigation, we were able to establish that the as-manufactured ultrathin nanoflakes film is composed of Co_3O_4. To provide further analysis on the microstructure of nanoflakes, Fig. S5a illustrates the TEM images of the film scraped from the substrate. From it a cross-linked framework can be clearly observed with arbitrarily curved flakes naturally connected with each other. Besides, the composition of pure flakes was measured by energy disperse spectroscopy (EDS), as illustrated in Fig. S6. In addition to signals which belong to the substrate, only two elements of Co and O can be detected (Fig. S6a). Combing with the elemental mapping result (Fig. S6b), We can further confirm that elements Co and O are evenly dispersed on NF. For advanced investigation, Fig. 1e and Fig. S5b illustrates high-close TEM images of Co_3O_4 flakes which contains both front-view (Fig. 1e) and side-view (Fig. S5b) observations. It can be seen from the front-view observation that the lying flake is nearly transparent to the electronic beam, which is indexed to the ultrathin structure of Co_3O_4. Besides, the thickness of flake could be precisely measured by the side-view image, with size of about 2.5 nm. Such an ultrathin thickness will undoubtedly make the Co_3O_4 nanoflakes possess a high active surface which is considered to be an ideal character for catalytic electrode. As for high-resolution TEM (HR-TEM) image displayed in Fig. 1f, the flake exhibits clear lattice fringes with interplanar spacing of 0.202 nm and 0.243 nm corresponding to the (400) and (311) planes of Co_3O_4. More additionally, a polycrystalline property of Co_3O_4 product was confirmed by the selected-area electron diffraction (SAED) pattern (insert of Fig. 1f). It depicts a series of diffraction rings that can be indexed to the diffractions of (311), (233), (400), and (440) crystal planes for spinel Co_3O_4. To further investigate the surface elemental valences, X-ray photoelectron spectroscopy (XPS) was employed to analyse the product and the corresponding curves are displayed in Fig. 1g-i. Fig. 1g depicts the wide-survey XPS spectrum while the high-resolution spectra of Co and O are given in Fig. 1h-i, respectively. The XPS profile of Co 2p (Fig. 1h) shows peaks corresponding to Co $2p_{1/2}$ and Co $2p_{3/2}$ along with three satellite peaks. The Co $2p_{1/2}$ can be deconvoluted into the peaks at 796.4 eV (attributed to Co^{2+}) and 794.4 eV (attributed to Co^{3+}), while the Co $2p_{3/2}$ peak could be fitted into the peaks at 781.4 eV (attributed to Co^{2+}) and 779.9 eV (attributed to Co^{3+})[31, 32]. As is indicated in Fig. 1i, the peak of O 1s is located at 529.9 eV and can be fitted into three peaks at 529.7 eV, 531.0 eV, and 532.3 eV which are assigned to lattice oxygen, oxygen vacancies and, chemisorbed oxygen, individually [33].

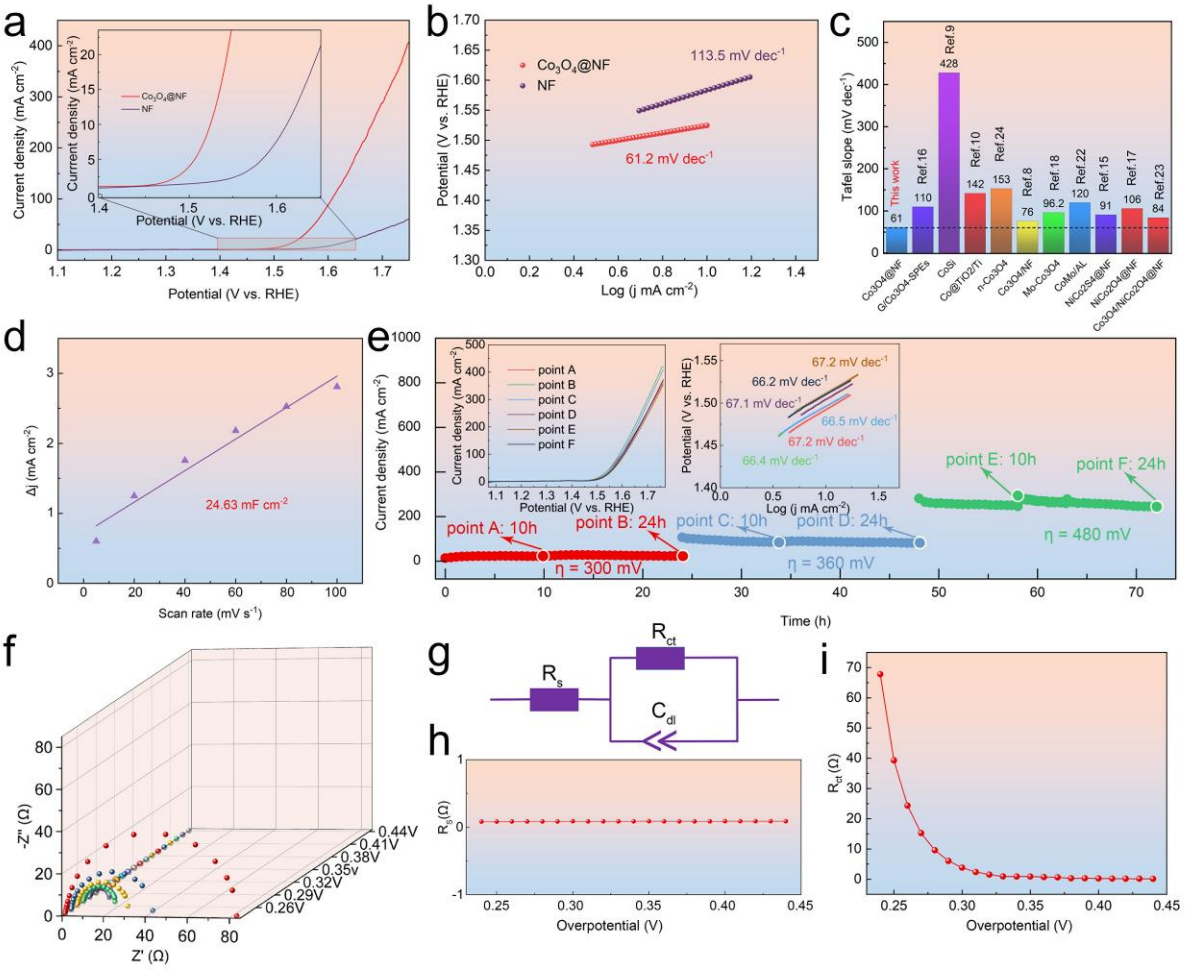

Figure 2. (a) The LSV curves (inset is high-resolution observation), and (b) corresponding Tafel slope curves of Co_3O_4@NF electrode and bare NF. (c) Comparison of Tafel slope on the recently reported Co-based electrodes. (d) Capacitive current density (Δ j) at 0.11 V versus RHE against the scan rate for Co_3O_4@NF electrode. (e) 72 h durability test of electrode at 1.53 V, 1.59 V and 1.71 V (vs RHE), separately (test for 24 hours at each potential). The insets show LSV curves collected at different points and relevant Tafel slopes, respectively. (f) 3D diagram of Nyquist plots, (g) equivalent circuit, (h) fitted R_s result and (i) fitted R_{ct} result of the *in situ* EIS test.

To demonstrate the performance of OER catalysis for Co_3O_4@NF electrode, Fig. 2a compares the linear sweep voltammetry (LSV) behavior of Co_3O_4@NF electrode with precursor NF at a scan rate of 5 mV s^{-1}. The enlarged plot in Fig. 2a indicates that the OER of Co_3O_4@NF electrode records the lowest onset potential of ~1.41 V (vs RHE), which is 120 mV lower than that of bare NF, indicating a high catalytic ability of ultrathin Co_3O_4 nanoflakes. Besides, a current of 10 mA cm^{-2} is obtained by Co_3O_4@NF electrode at the overpotential (η) of 290 mV. Compared with that of bare NF (380 mV) and previous reported materials (as is shown in Table 1) [16-18, 22-24, 34-36], it is apparent that the as-synthesized Co_3O_4@NF electrode exhibited enhanced OER catalytic ability. Moreover, according to LSV result, the Tafel slopes of Co_3O_4@NF electrode and NF are calculated in Fig. 2b.

Table. 1 A comparison on the OER catalytic performances of recently reported Ni-based@NF film electrodes.

	Electrode	Electrolyte	η_j[a]（mV）	Reference
1	Co_3O_4@NF	6M KOH	η_{10}=290	This work
2	Co/NF	1M NaOH	η_{10}=410	15
3	G/Co_3O_4-SPEs	1M KOH	η_{10}=304	16
4	CoMo/AL	1M KOH	η_{10}=361	17
5	NiCoMoSe	1M KOH	η_{10}=390	18
6	$NiCo_2O_4$@NF	1M KOH	η_{10}=364	22
7	CoSi	50g/L H_2SO_4	η_{10}=783	23
8	c-Co_3O_4	1M KOH	η_{10}=440	24
9	rGO/NF	1M KOH	η_{10}=347.45	34
10	Co sphere	1M KOH	η_{10}=430	35
11	xAg_2O-yPrO_2/γ-Al_2O_3	1M KOH	η_{10}=422	36

[a] η is the overpotential, and j is the current density of electrode with unit of mA cm^{-2}.

Table. 2 A comparison on the OER catalytic performances of recently reported Ni-based@NF film electrodes.

	Electrode	Electrolyte	Tafel slope（mV dec^{-1}）	Reference
1	Co_3O_4@NF	6M KOH	61	This work
2	Co_3O_4/NF	1M KOH	76	8
3	CoSi	50g/L H_2SO_4	428	9
4	Co@TiO_2/Ti	1M KOH	142	10
5	$NiCo_2S_4$@NF	1M NaOH	91	15
6	G/Co_3O_4-SPEs	1M KOH	110	16
7	NiCoMo	1M KOH	83	17
8	Mo-Co_3O_4 NFs	1M KOH	96.2	18
9	Co_3O_4-Mo_2N-NFs	1M KOH	87.8	18
10	CoMo/AL	1M KOH	120	22
11	$NiCo_2O_4$@NF	1M KOH	106	22
13	Co_3O_4/$NiCo_2O_4$@NF	0.1M KOH	84	23
14	n-Co_3O_4	1M KOH	153	24

The fitted value of 61.2 mV dec^{-1} for Co_3O_4@NF is much lower than that of bare NF (113.5 mV dec^{-1}) as well as most of previously reported Co-based materials (Fig. 2c and Table 2) [8-10, 15-18, 22-24]. To better understand the electrocatalytic activity of the as-prepared electrode, cyclic voltammetry

(CV) tests at different scan rates were performed (Fig. S7). The current density at median potential (0.11 V. vs RHE) is linearly fitted with scan rate to obtain the electrochemical double layer capacitance (C_{dl}) denoting the effective electrochemical surface area (ECSA). It can be clearly observed from Fig. 2d that the C_{dl} of Co_3O_4@NF electrode is 24.63 mF cm^{-2}, which reflects its excellent catalyst performance. The exceptional performance of the product herein could be attributed to the advanced structure of anchored Co_3O_4 nanoflakes, which possesses the following advantages: Firstly, the as-grown nanoflakes could avoid particles aggregation and show a strong affinity as well as improved electronic conductivity with substrate. Secondly, the ultrathin structure makes the product a substantial high specific surface area which will form a large quantity of catalytic sites and facilitate the best performance of active materials.

Moreover, the durability of the as-synthesized electrode for OER catalysis was determined via a 72 h chronoamperometry (CA) test at various polarizations potentials. Fig. 2e depicts the current density-time curve when the overpotential is set at 300 mV, 360 mV, and 480 mV for 24 h, respectively. The electrode possesses current densities of 20 mA cm^{-2} (300 mV), 97.5 mA cm^{-2} (360 mV), and 278.8 mA cm^{-2} (480 mV) at the initial stage, and could keep stable for 24 h, respectively. The LSV curves collected at each potential after every 10 h and 24 h test (marked as points A-F) as well as the homologous Tafel slopes are illustrated in the insets of Fig. 2e. Few obvious changes indicate the excellent durability of the electrode for long-term running. All the electrochemical tests demonstrate that the as-synthesized product perform excellently for OER catalysis with enhanced activity and durable stability. As shown in Fig. 2f and Fig. S8, the kinetic characteristic of the Co_3O_4@NF electrode is studied using *in situ* EIS technology in order to determine the root cause for its enhanced OER catalytic activity. Fig. 2g indicates the relevant equivalent circuit model. The intercept of the plot with the X-axis in the higher-frequency area of the Nyquist plot is the equivalent series resistance (R_s). It's represented the solution resistance and contact resistance. Furthermore, the semicircle's diameter reflects the charge transfer resistance (Rct), which is contributed by the reaction resistance of OER [1, 2, 4, 21]. As the overpotential increases from 240 mV to 440 mV, the R_s always remained at a stable value, reflecting excellent compatibility on the electrolyte/electrode interface (Fig. 2h). Besides, the fitted R_{ct} value of Co_3O_4@NF electrode displays dramatically decline from 67.81 Ω to 0.44 Ω (Fig. 2i). It is worth noticing that the tendency of the sharp decline of R_s obviously decelerates after the overpotential approach 290 mV. This is exactly consistent with the overpotential when the current density begins to increase significantly in LSV. This phenomenon further indicates the outstanding compatibility as well as self-adaptability of the electrode for OER catalysis, which is related to the considerably declined overall resistance.

In addition, to further verify the performance of the electrode in practical water splitting application, a single electrolysis cell (inset in Fig. 3a) was assembled with Co_3O_4@NF electrode as anode, and Pt@NF electrode (the corresponding characterization is given in Fig. S1) as cathode. Based on the LSV test, the practical water splitting voltage of Co_3O_4@NF||Pt@NF cell displays ~1.50 V to achieve a typical current density of 10 mA cm^{-2}, and peak current density of 290 mA cm^{-2} is exhibited at 2.0 V (inset in Fig. 3a). In addition, the steady result of CA test (Fig. 3a) under the applied voltage as high as 1.9 V for 24 h and the stable LSV curves obtained at 4 and 24 h respectively throughout the test (inset of Fig. 3a) show that the Co_3O_4@NF electrode possesses extremely efficient OER activity.

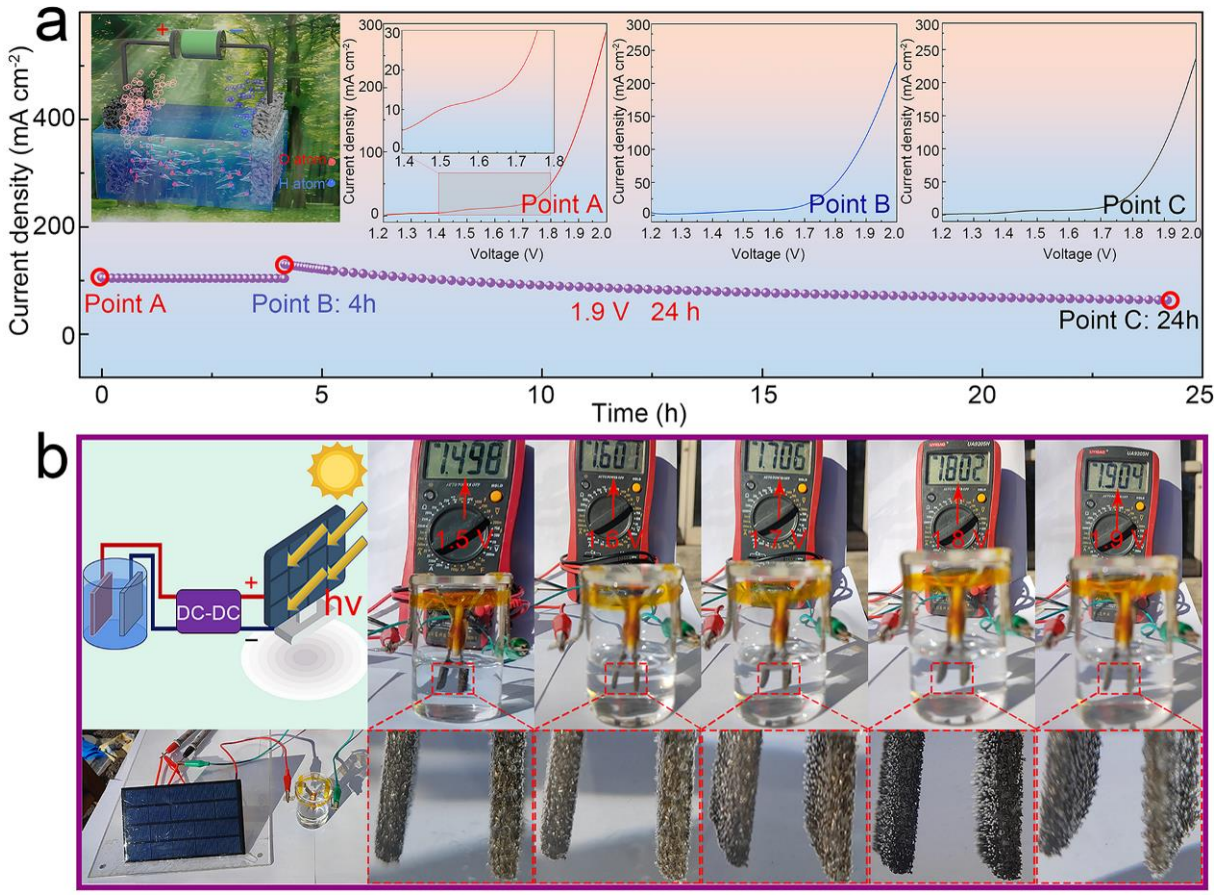

Figure 3. (a) The 24 h durability test of Co_3O_4@NF || Pt@NF cell. Insets are the schematic illustration of a single electrolysis cell and the LSV curves tested at different points. (b) The test of Co_3O_4@NF || Pt@NF cell on a solar cell-H_2O splitting electrolyzer station.

Moreover, taking the practical application into consideration, a solar cell-H_2O splitting electrolyzer station was constructed by connecting commercial solar cell (5 V,1 A) to our single cell via a DC-DC converter, as illustrated in Fig. 3b. When exposed in sunlight at test voltages ranging from 1.5 V to 1.9 V, the electrolysis reaction intensifies as the cell voltage rises. Meanwhile, the obvious gas evolution can be witnessed which is relevant to the splitting of water to H_2 and O_2 at the cathode and anode, respectively. This result reveals the practical application value of the Co_3O_4@NF electrode.

4. CONCLUSION

In conclusion, a simple technique is effectively used to create a Co_3O_4@NF electrode with Co_3O_4 nanoflakes that have an intrinsic cross-linked structure and an ultrathin thickness of roughly 2.5 nm. The product benefits from a high active surface area, strong affinity, and good conductivity as a result of its as-grown structure and ultrathin property. Utilized as additive-free electrode for OER catalysis, it displays a low overpotential of 290 mV at 10 mA cm^{-2} with a small Tafel slope of 61.2 mV dec^{-1} as well as remarkable durable stability for 72 h long-term running under various potentials. Additionally, *in situ* EIS is adapted to further verify its compatibility and self-adaptability for OER catalysis. The as-

fabricated electrolyzer obtains a current density of 290 mA cm^{-2} at 2 V and demonstrates superior long-term stability. Combined with its excellent performance in the solar cell-H_2O splitting system, the Co_3O_4@NF electrode illustrates marvelous capability in practical application. More notably, the adopted simple approach may provide a promising way to fabricate other high-performance ultrathin NPs for OER catalysis.

CONFLICTS OF INTEREST

The authors declare that they have no known competing financial interests or personal relationships that could have appeared to influence the work reported in this paper.

ACKNOWLEDGEMENTS

This work was supported by the Hebei Province Natural Science Foundation (No. B2022203008).

SUPPORTING MATERIALS

1. Calculations

The reported potential reference reversible hydrogen electrode (RHE) was calculated according to the following equation:

$$E_{RHE}=E_{Ag/AgCl}+0.197+0.0591\times pH \quad (S1)$$

The Tafel slope of the electrode was calculated via the following Tafel equation:

$$\eta=a+b\times \log j \quad (S2)$$

where η is the overpotential (V), j is the current density (mA cm^{-2}) and b is the Tafel slope (mV dec^{-1}).

2. Supporting Figures

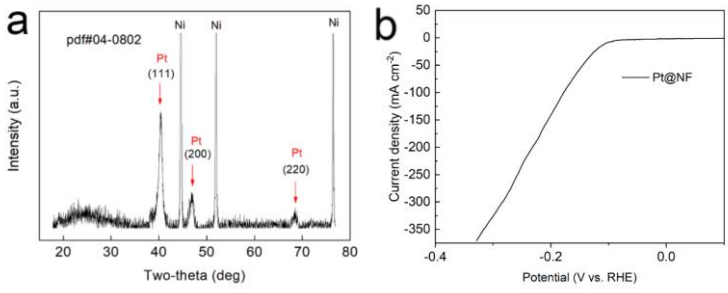

Fig. S1 (a) XRD pattern of as-synthesized Pt@NF electrode (on a Rigaku Smart Lab X-ray diffractometer operated at 40 kV with Cu Kα radiation under a scan rate of 5° min^{-1}), and (b) the LSV curve of single Pt@NF electrode in 6M KOH at the scan rate of 5 mV s^{-1}

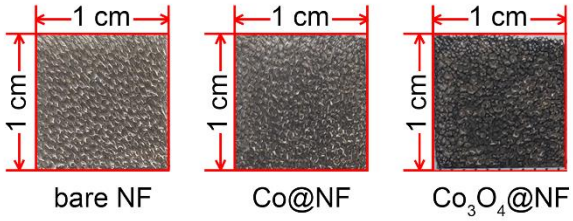

Fig. S2 The comparisons of digital images which are bare NF, original Co@NF and Co_3O_4@NF, respectively (all of them were pictured in natural light).

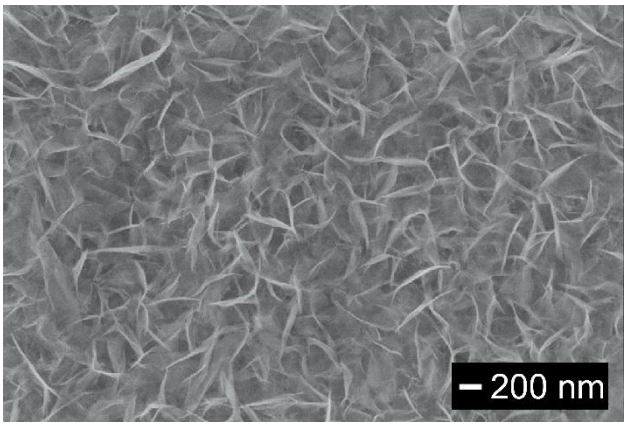

Fig. S3 Low-magnification SEM image of as-obtained Co_3O_4 film product (tested on a Hitachi S-4800 instrument operated at 5 kV).

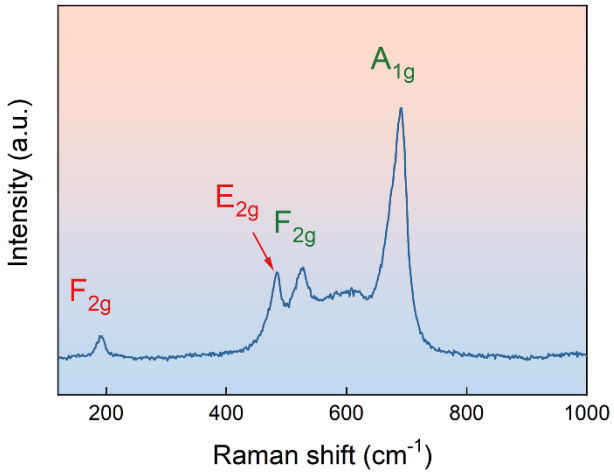

Fig. S4 Typical Raman spectra of original Co_3O_4@NF electrode (on a Renishaw invia system with an excitation wavelength of 514 nm).

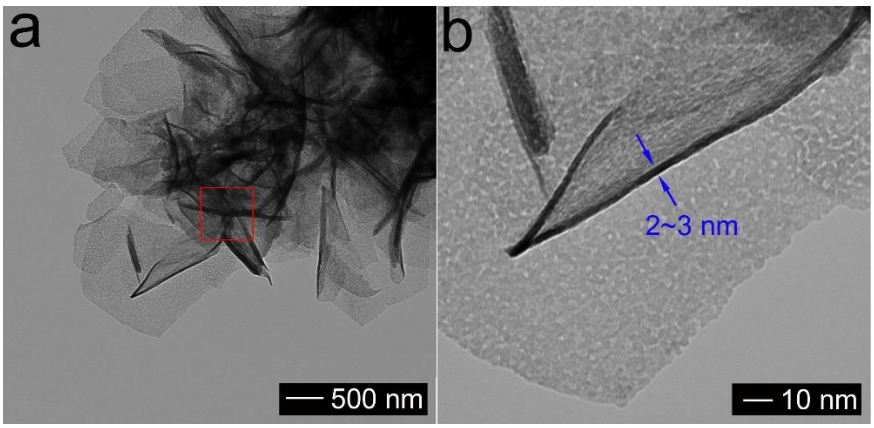

Fig. S5 High-close TEM images of Co_3O_4 flakes which contain both (a) front-view (b) and side-view observations (on a Philips Tecnai G2 F30 operated at 300 kV).

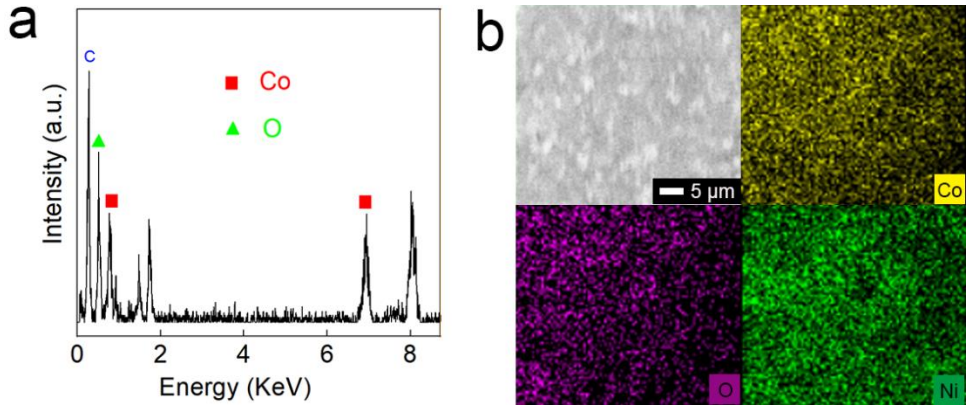

Fig. S6 The EDS spectra and corresponding elemental mapping of as-obtained product (tested on a Hitachi S-4800 instrument operated at 5 kV).

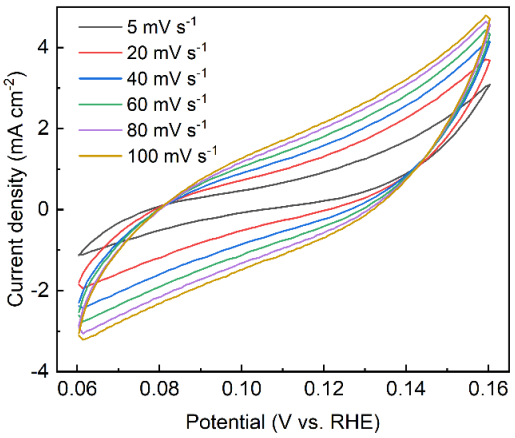

Fig. S7 CV curves of Co_3O_4@NF were tested at different scan rates from 5 mV s^{-1} to 100 mV s^{-1} in 6M KOH system.

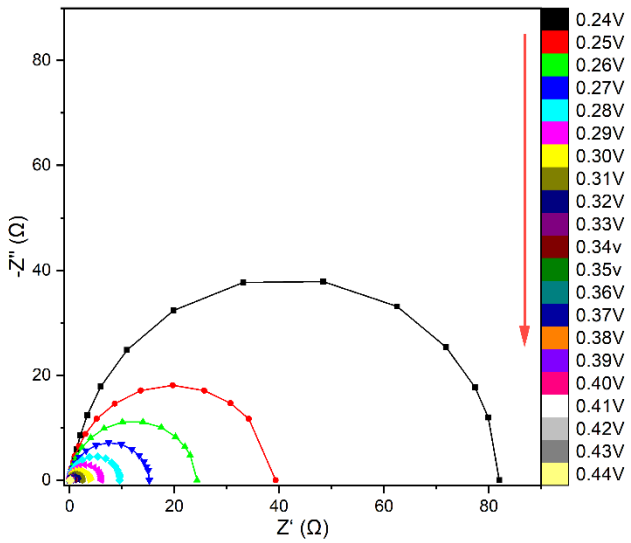

Fig. S8 The original *in situ* EIS spectra of the Co_3O_4@NF electrode during various potentials from 0.24V to 0.44V (with a sampling interval of 0.01 in 6M KOH).

References

1. Y. Li, X. Wei, L. Chen, J. Shi, *Angew. Chem. Int. Ed. Engl.*, 60 (2021) 19550-19571.
2. Y.Z. Wang, M. Yang, Y.M. Ding, N.W. Li, L. Yu, *Adv. Funct. Mater.*, 32 (2021) 2108681.
3. L. She, G. Zhao, T. Ma, J. Chen, W. Sun, H. Pan, *Adv. Funct. Mater.*, 32 (2021) 2108465.
4. J.N. Hausmann, R. Beltran-Suito, S. Mebs, V. Hlukhyy, T.F. Fassler, H. Dau, M. Driess, P.W. Menezes, *Adv. Mater.*, 33 (2021) 2008823.
5. N. Liu, Q. Zhang, J. Guan, *Chem. Commun.*, 57 (2021) 5016-5019.
6. M. Zhang, Y. Zhang, L. Ye, B. Guo, Y. Gong, *Applied Catalysis B: Environmental*, 298 (2021) 120601.
7. M. Yu, E. Budiyanto, H. Tuysuz, *Angew. Chem. Int. Ed. Engl.*, 61 (2022) 202103824.
8. D. Tang, Y. Ma, Y. Liu, K. Wang, Z. Liu, W. Li, J. Li, *J. Alloys Compd.*, 893 (2022) 162287.
9. B. Shen, Y. He, Z. He, Z. Wang, Y. Jiang, H. Gao, *J. Colloid Interface Sci.*, 605 (2022) 637-647.
10. C. Yang, C.M. Makabu, X. Du, J. Li, D. Sun, G. Liu, *Electrochim. Acta*, 396 (2021) 139213.
11. G.S. Hutchings, Y. Zhang, J. Li, B.T. Yonemoto, X. Zhou, K. Zhu, F. Jiao, *J. Am. Chem. Soc.*, 137 (2015) 4223-4229.
12. Q. Zhang, Z. Duan, M. Li, J. Guan, *Chem. Commun.*, 56 (2020) 794-797.
13. Z. Wang, Z. Lin, P. Diao, *Chem. Commun.*, 55 (2019) 3000-3003.
14. J. Qi, J. Xie, Z. Wei, S. Lou, P. Hao, F. Lei, B. Tang, *Chem. Commun.*, 56 (2020) 4575-4578.
15. X. Yin, G. Sun, L. Wang, L. Bai, L. Su, Y. Wang, Q. Du, G. Shao, *Int. J. Hydrogen Energy*, 42 (2017) 25267-25276.
16. N. Srinivasa, L. Shreenivasa, P.S. Adarakatti, R.D. Crapnell, S.J. Rowley-Neale, A. Siddaramanna, C.E. Banks, *Int. J. Hydrogen Energy*, 45 (2020) 31380-31388.
17. L. Yang, B. Zhang, B. Fang, L. Feng, *Chem Commun (Camb)*, 54 (2018) 13151-13154.
18. T. Wang, P. Wang, W. Zang, X. Li, D. Chen, Z. Kou, S. Mu, J. Wang, *Adv. Funct. Mater.*, 32 (2021) 2107382.
19. R. Zhang, Z. Sun, C. Zong, Z. Lin, H. Huang, K. Yang, J. Chen, S. Liu, M. Huang, Y. Yang, W. Zhang, Q. Chen, *Nano Energy*, 57 (2019) 753-760.
20. Q. Ren, J.-Q. Wu, C.-F. Li, L.-F. Gu, L.-J. Xie, Y. Wang, G.-R. Li, *Chem. Commun.*, 57 (2021)

1522-1525.
21. S. Du, Z. Ren, J. Zhang, J. Wu, W. Xi, J. Zhu, H. Fu, *Chem Commun (Camb)*, 51 (2015) 8066-8069.
22. B.K. Martini, L.S. Bezerra, S. Artemkina, V. Fedorov, P.K. Boruah, M.R. Das, G. Maia, *Chemical Engineering Journal Advances*, 9 (2022) 100206.
23. M. Yang, W. Lu, R. Jin, X.-C. Liu, S. Song, Y. Xing, *ACS Sustainable Chemistry & Engineering*, 7 (2019) 12214-12221.
24. C. Alex, S.C. Sarma, S.C. Peter, N.S. John, *ACS Applied Energy Materials*, 3 (2020) 5439-5447.
25. F.-Y. Chen, Z.-Y. Wu, Z. Adler, H. Wang, *Joule,* 5 (2021) 1704-1731.
26. B. Wu, Z. Yang, X. Dai, X. Yin, Y. Gan, F. Nie, Z. Ren, Y. Cao, Z. Li, X. Zhang, *Dalton Trans*, 50 (2021) 12547-12554.
27. D. Lyu, Y. Du, S. Huang, B.Y. Mollamahale, X. Zhang, S.W. Hasan, F. Yu, S. Wang, Z.Q. Tian, P.K. Shen, *ACS Applied Materials & Interfaces*, 11 (2019) 39809-39819.
28. H.S. Stein, D. Guevarra, A. Shinde, R.J.R. Jones, J.M. Gregoire, J.A. Haber, *Materials Horizons*, 6 (2019) 1251-1258.
29. Z. Li, Z. Wang, S. Xi, X. Zhao, T. Sun, J. Li, W. Yu, H. Xu, T.S. Herng, X. Hai, P. Lyu, M. Zhao, S.J. Pennycook, J. Ding, H. Xiao, J. Lu, *ACS Nano*, 15 (2021) 7105-7113.
30. S.-F. Hung, C.-W. Tung, T.-S. Chan, H.M. Chen, *CrystEngComm*, 18 (2016) 6008-6012.
31. X. Fan, Y. Xu, C. Ma, W. He, *J. Alloys Compd*., 854 (2021) 157234.
32. Z. Zhu, G. Lu, Z. Zhang, Y. Guo, Y. Guo, Y. Wang, *ACS Catalysis*, 3 (2013) 1154-1164.
33. Z. Xiao, Y.C. Huang, C.L. Dong, C. Xie, Z. Liu, S. Du, W. Chen, D. Yan, L. Tao, Z. Shu, G. Zhang, H. Duan, Y. Wang, Y. Zou, R. Chen, S. Wang, *J. Am. Chem. Soc*., 142 (2020) 12087-12095.
34. K. Shah, R. Dai, M. Mateen, Z. Hassan, Z. Zhuang, C. Liu, M. Israr, W.C. Cheong, B. Hu, R. Tu, C. Zhang, X. Chen, Q. Peng, C. Chen, Y. Li, Angew. Chem. Int. Ed. Engl., 61 (2022) 202114951.
35. F. Zeng, C. Mebrahtu, L. Liao, A.K. Beine, R. Palkovits, Journal of Energy Chemistry, 69 (2022) 301-329.
36. M. Khan, N.K. Janjua, A. Ahmad, R. Luque, A.A. Al‐Kahtani, A.M. Tighezza, International Journal of Energy Research, 46 (2022) 14161-14173.